Microfluidic Mixing Device With Integrated Dual-Band Microwave Sensor

Máté Kálovics, Kristóf Iván, *Member, IEEE*, and Zsolt Szabó, *Member, IEEE*

***Abstract*—A microfluidic mixer is integrated with a dual-band microwave resonator to allow in situ monitoring of mixing two liquids. The resonator is a complementary double split-ring resonator, which is etched in the ground plane of a microstrip transmission line. The output channel of the mixer is conducted below the ground plane in the near field of the resonator. Electromagnetic and fluid dynamic simulations have been performed to design optimal channel configurations for this section to increase the sensitivity, minimize the volume of the required liquid sample, and eliminate unwanted microfluidic mixing. The frequency variation of the first two resonances is monitored by measuring the transmission parameter of the microstrip line. The performance of the device is demonstrated by mixing saline solutions of different concentrations and the transmission spectra of different chemicals are also presented. It is shown that the device can allow unambiguous chemical identification by simultaneous monitoring of the two resonances. The total amount of fluid required to operate the device is less than 8 μL.**

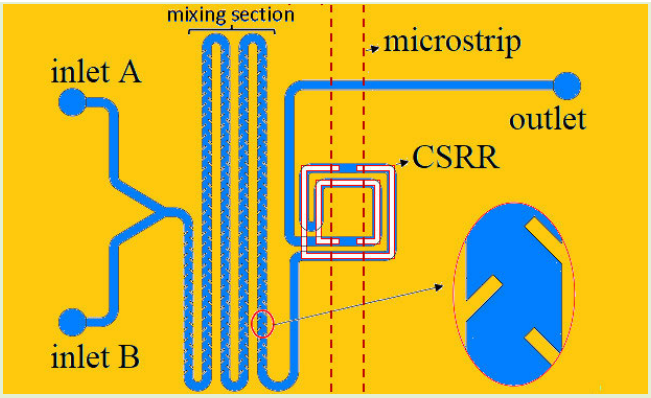

***Index Terms*—Chemical and biological sensors, microfabrication, microfluidics, microwave sensors, split-ring resonators (SRRs).**

I. Introduction

MICROFLUIDICS allows the precise control and manipulation of fluids on a very small scale, that is at μL or even nL volumes. Nowadays, complex lab-on-a-chip devices are developed, which integrate many functions, such as sample preparation, assay manipulation, and reactions [1], [2]. These functions are supplemented with sensing and detection in order to monitor the microfluidic processes and to allow the readout of the results. The goals of Industry 4.0 includes the development of small-sized sensors, which may find applicability in lab-on-a-chip technologies and can lead to the widespread use of these devices. Recently, significant efforts have been devoted to resonance-based microwave sensing, especially for linear and angular displacement monitoring [3], [4] and material characterization in the fields of biosensing [5], [6], agriculture [7], [8], medicine, and pharmaceutical industry [9], [10]. Different regimes of the electromagnetic spectrum present distinct advantages for sensing and can provide complementary information about the samples to be perceived. Therefore, to increase the reliability and accuracy, dual technology sensors have been developed, where often a microwave sensor is supplemented with an infrared or optical sensor [11], [12], [13], [14]. Resonance-based microwave sensors have high precision and reliability; they can operate in harsh environmental conditions [3]. During the more than two decades of metamaterial research, many subwavelength resonator geometries have been investigated to produce engineered electromagnetic response [15], [16]. Among them, split-ring resonators (SRRs) and their variants are the most examined structures as being a suitable candidate to engineer customized magnetic properties from microwave up to terahertz frequencies [16], [17]. By employing Babinet's principle, the dual structure, called complementary SRR (CSRR), has also been proposed [15], [18]. SRRs and their variants have been applied as backward wave structures for directional emission [15], in microwave filters [18], as sensing elements [19], for the characterization of planar dielectric materials [20], [21], [22], and as fluidic sensors [10], [23], [24], [25], [26], [27], [28], [29], [30].

Despite so many applications of microwave sensors, in the case of microfluidic lab-on-a-chip devices, there are additional challenges to be addressed, which to our knowledge, have not yet been adequately discussed in the literature. First, small amounts of liquids must be detected. However, not only the sensor sensitivity is the most important aspect, but also

Manuscript received 30 March 2023; revised 25 April 2023 and 18 May 2023; accepted 18 May 2023. Date of publication 1 June 2023; date of current version 14 July 2023. This work was supported by the National Research, Development and Innovation Office of Hungary (NKFIH) under Grant K-132050. The associate editor coordinating the review of this article and approving it for publication was Dr. Wensong Wang. *(Corresponding author: Zsolt Szabó.)*

The authors are with the Faculty of Information Technology and Bionics, Pázmány Péter Catholic University, 1083 Budapest, Hungary (e-mail: szabo.zsolt@itk.ppke.hu).

Digital Object Identifier 10.1109/JSEN.2023.3280240

other considerations related to fluid flow must be considered. Therefore, the design of the fluidic channel in the sensing area requires special considerations. On the other hand, the microfluidic lab-on-a-chips can have complex densely packed geometries, where sensing is required at different locations. It is essential that the properties of the liquids flowing in the channels, which are outside of the sensing area, do not cause unwanted influence. Such sensors are required where the geometry of the fluidic channels does not have to be redesigned. Finally, to allow identification of fluids based on the dispersion of their electric permittivity, the sensor is required to work in at least two frequency bands.

The microfluidic systems transport and process fluids, and one of the typical operations is mixing. Homogeneous mixing of liquids is essential in many processes, but due to the low Reynolds number of laminar flow, it is difficult to achieve it in microfluidics. Passive mixing techniques, which utilize precisely designed channel geometries for mixing, are suitable in a lab-on-a-chip environment and are also suitable for integration with microwave sensors. Microfluidic mixers can have simple tortuous/zigzag channels [31] or more complicated designs with additional structuring [32], [33], [34], [35].

In this article, a transmission-based microwave sensor is integrated into a microfluidic mixer in a lab-on-a-chip configuration. The sensor, which is a CSRR, is located in the ground plane of a microstrip transmission line and monitors the properties of the mixed fluid. The design and fabrication procedure is described and prototypes are presented. Electromagnetic and fluid dynamics simulations are jointly applied to design the optimized fluidic channel, which guides the liquid properly to the sensing area, and at the same time, it provides the required sensitivity of the sensor. The performance of the device is demonstrated by mixing saline solutions of different concentration and the transmission spectra of several chemicals are also presented. A comparison with existing state-of-the-art resonance base microwave fluidic sensors is provided.

II. Design of the Device

The sketch of the device geometry is presented in Fig. 1. It consists of a microstrip transmission line with a ground plane, in which a CSRR is etched and the microfluidic layer placed below. The fluidic channels are fabricated in polydimethylsiloxane (PDMS) and they are covered with a 150-μm-thick borosilicate glass. The fluidic layer is glued to the bottom of the ground plane with a thin PDMS layer (approximately 55 μm in thickness). The dimensions of the device are summarized in Table I. The size of the device is $s_x = 35$ mm and $s_z = 45$ mm. The substrate is 0.76-mm-thick ISOLA IS680-345 [36], with 38-μm copper cladding. The mixer has two inlets (A and B) and one outlet. The width of the fluidic channels is 500 μm and the height is 100 μm along its full length. The total length of the mixing section is 81 mm. Below the CSRR, that is, in the sensing region, the fluidic channel is designed to cover the most surface area, as it can be observed in Fig. 1(d). The thickness of the fluidic layer is 2 mm.

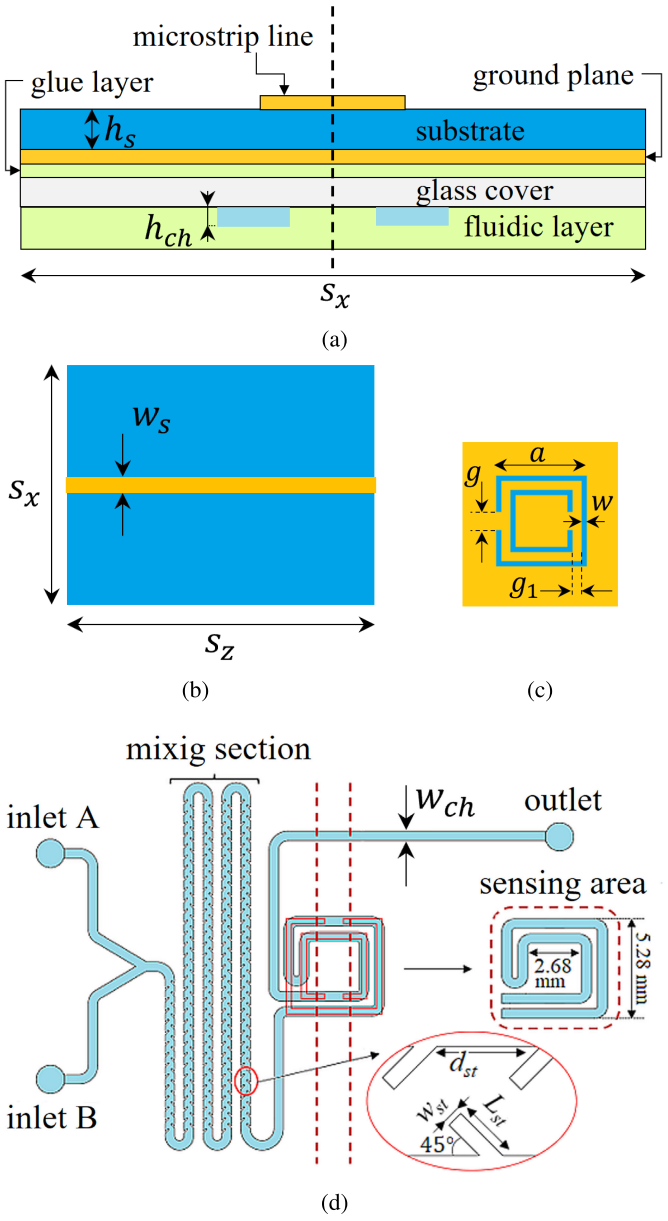

Fig. 1. Geometry of the mixing device with the CSRR sensor. (a) Schematic cross section. (b) Top of the sensor with the microstrip line. (c) Ground plane with the CSRR. (d) Geometry of the fluidic layer.

A. Design of the Dual-Band Microwave Resonator

The electromagnetic behavior of SRR and CSRR has been extensively studied [16], [37], [38], [39], including coupling and excitation of different modes [40], [41]. The first two modes of the double CSRR possess perfect magnetic conductor (PMC) symmetry (where $H_t = 0$) along the geometrical symmetry plane [42]. The fundamental propagating mode of the microstrip line has the PMC symmetry. Therefore, it can excite the first two modes of the CSRR when their symmetry planes are aligned. By loading the microstrip transmission line with the CSRR the transmission parameter exhibits stopband behavior at resonant frequencies, where the injected power is mostly reflected.

The microwave resonator is designed with the frequency-domain solver of the commercial software CST Microwave

TABLE I
MAIN DIMENSIONS OF THE DEVICE

s_x (mm)	s_y (mm)	h_s (mm)	ϵ_r	$\tan\delta$
35	45	0.76	3.45	0.0035
w_s (mm)	g_1 (mm)	g (mm)	w (mm)	a (mm)
1.7	0.5	1.0	0.3	5.08
w_{ch} (μm)	h_{ch} (μm)	L_{st} (μm)	w_{st} (μm)	d_{st} (μm)
500	100	273	75	480

Studio. The ISOLA substrate is modeled as lossy dielectric with electric permittivity $\epsilon_r = 3.45$ and loss tangent $\tan\delta = 0.0035$. The copper is considered as lossy metal with the electric conductivity of $5.8 \cdot 10^7$ S/m. The thickness of the microstrip line is $w_s = 1.7$ mm, which can provide a good transmission of the unloaded transmission line over the frequency range of 2–12 GHz. To facilitate fabrication, the following dimensions of the CSRR are fixed: the distance between the inner and outer ring is $g_1 = 0.5$ mm, the binding is $g = 1$ mm, and the width of the etched rings is $w = 0.3$ mm. The size of the outer ring is obtained with optimization so that the first resonance of the CSRR is at 5 GHz, which results in $a = 5.08$ mm [43]. Two samples are fabricated and their S_{21} transmission parameter is measured with a two-port P9374A Keysight vector network analyzer. The measured and simulated S_{21} parameters are compared in Fig. 2(a). The measured data show a good agreement except for a small frequency shift compared to the simulation.

The simulated electric field distributions at the first (5 GHz) and second (10.432 GHz) resonance are presented as well. The field distributions of Fig. 2(b) and (d), that is, the cross section just below the ground plane, shows that both modes have PMC symmetry along which the maximum field intensity occurs. The electric field distributions of Fig. 2(c) and (e) are plotted along the symmetry plane of the sensor. The near field of both resonances extends well below the ground plane; consequently, they can be utilized for sensing. However, the extent of the second mode is more localized. The operation of the CSRR can be understood by considering a single slot, which is cut in the ground plane and positioned symmetrically to the microstrip line. In the case of the first mode, the maximum electric field intensity occurs at the middle of the slot and it decreases to null at the two ends. It can be shown that the essential electromagnetic characteristics do not change by folding the slot, for example, in the shape of a single CSRR. The purpose of folding is to make the geometry compact, and it can also increase the quality factor of the resonator. The double CSRR can be thought of as two closely spaced folded slots with different lengths where the previous statement is still valid, but couplings are also created between the slots. In the case of the second resonance [see Fig. 2(c)], it is clearly observable that the maximum electric field intensity occurs at the middle of the inner ring shaped slot and decreases to zero at the ends. Similarly, in the case of the first resonance [see Fig. 2(b)], the maximum field intensity occurs at the middle of the outer ring, but due to inductive coupling, the inner ring is also excited. In the case of double SRR/CSRR metamaterials, this hybrid mode excitation is responsible for the bianisotropy.

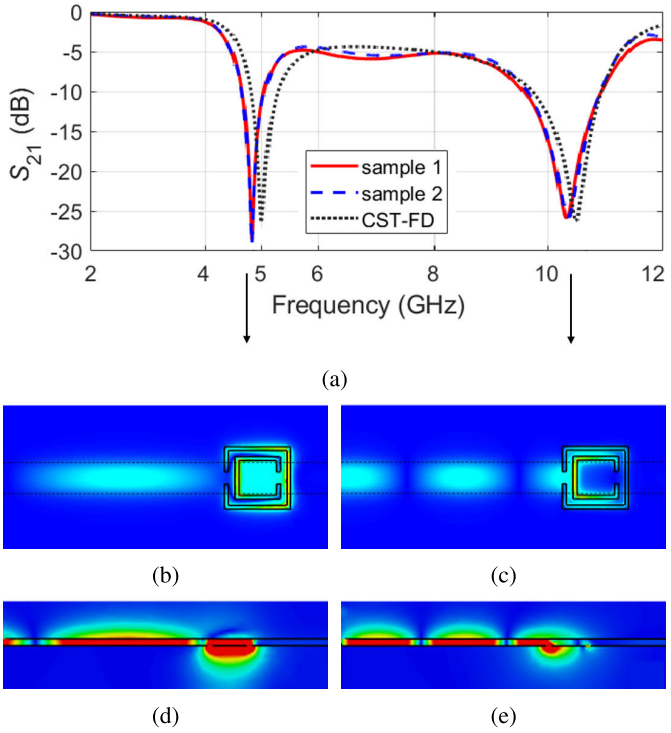

Fig. 2. (a) Measured and simulated S_{21} transmission parameter of the microwave resonator. The simulations are performed with the frequency-domain solver of CST Microwave Studio. Electric field distributions at (b) and (d) first resonance (5 GHz) and (c) and (e) second resonance (10.432 GHz).

B. Design of the Fluidic Sections

The geometry of the microfluidic mixer is presented in Fig. 1(d). It consists of two inlets (A and B), a junction, a mixing section, a sensing area, and an outlet. The liquids with different properties are introduced continuously into the mixing section. The microchannels have a rectangular cross section, the width is $w_{\text{ch}} = 500$ μm, and the height is $h_{\text{ch}} = 100$ μm. The total length of the mixing section is 81 mm and the periodic guiding columns in it are $L_{\text{st}} = 273$ μm long and $w_{\text{st}} = 75$ μm wide, positioned at 45° angle to the channel wall. The distance between two guiding columns is $d_{\text{st}} = 480$ μm. The two fluids mix with each other due to the winding geometry of the channel and the guiding columns in it, which cause a "zig-zag" motion of the flow. The tortuous channel causes the mixing of liquids by changing their flow direction. The guiding columns in it facilitate this process making the fluid to flow along a meandering path even on the otherwise straight sections. The volume ratio of the fluids can be changed by controlling the pressure of the two inlets. Good mixing can be achieved in two regimes when the total flow rate is under 0.2 mL/h or when it is larger than 40 mL/h, as it can be seen in Fig. 3. Furthermore, as shown in Fig. 4(e) in the intercolumnar regions, vortices are formed, which further enhances the mixing. In essence, these vortices act as a mechanical mixer [32].

The mixing section is then transitioned to the sensing area, which is behind the ground plane in the near field of the CSRR. The pattern of the channel is selected based on the following reasons. The spectral positions of the CSRR

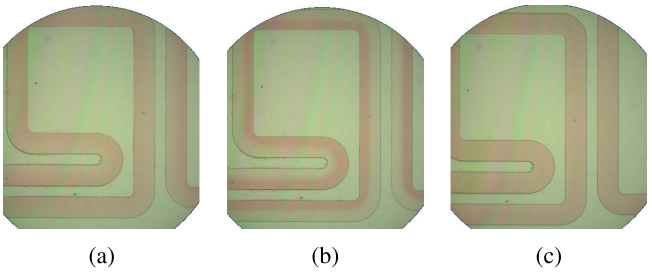

Fig. 3. Microscope images of fluid mixing at different flow rates. (a) Total flow rate is 0.2 mL/h and the fluids are mixing due to diffusion mostly. (b) Total flow rate is 10 mL/h and the mixing is only partial. (c) Total flow rate is 40 mL/h and the fluids are completely mixed under the influence of inertial forces.

resonance are influenced by the electric permittivity of the fluid flowing in the microchannel. Thus, by measuring their displacement relative to a reference, we can obtain information about the properties of the liquid. The sensitivity of the sensor depends on the amount of fluid in the near field of the CSRR (see Fig. 2). By inspecting the extent and the distribution of the near field, the obvious solution to achieve high sensitivity is to create a fluidic reservoir below the CSRR. However, not only sensitivity is the parameter, which must be considered. In many cases, the available sample is limited, so it is necessary to design a fluidic device with the smallest possible volume but with sufficient sensitivity. In addition, by changing the properties of input fluids, the mixture to be measured is formed over time as a result of a transient process since the liquid in the channel must first flow out. Therefore, special considerations must be taken how the fluid is handled in the sensing region to avoid contamination with the previous sample and unwanted mixing. As it is shown next, the appropriate solution is not a reservoir, but a properly guided fluidic channel below the CSRR. To find the optimized channel configuration in the sensing region, computational fluid dynamics simulations of different geometries are performed with the commercial software Comsol Multiphysics. The time-dependent transport solver of diluted species embedded in laminar flow has been utilized. In the simulations, 10-ppt saline water is considered on inlet A and distilled (0 ppt) water on inlet B at a flow rate of 20 mL/h each. Some of the investigated geometries are shown in Fig. 4. For each of these geometries, the concentration variation along the cross section of the sensing area [see the dotted line of Fig. 4(a)–(e)] is presented in Fig. 4(f). In Fig. 4(a)–(c) where the transition of the mixing section widens into the reservoir the concentration of salty water ranges from 1 to 5 ppt. With increasing the aspect ratio of the channel, the velocity of the fluid is rapidly decreasing and vortices are created in the corners of the reservoir. These vortices trap liquid, which can result in unwanted mixing and insignificant data readout. Furthermore, during filling of the channel, air bubbles can get stuck in the corners of the reservoir, which can also lead to incorrect results. To avoid these two effects, the use of simple channels is required. In the case of Fig. 4(d) and (e), there is no reservoir utilized in the sensing area and the concentration of mixed fluid is the same, 5 ppt constantly along the channel. Therefore, the channel configuration of Fig. 4(e) is selected

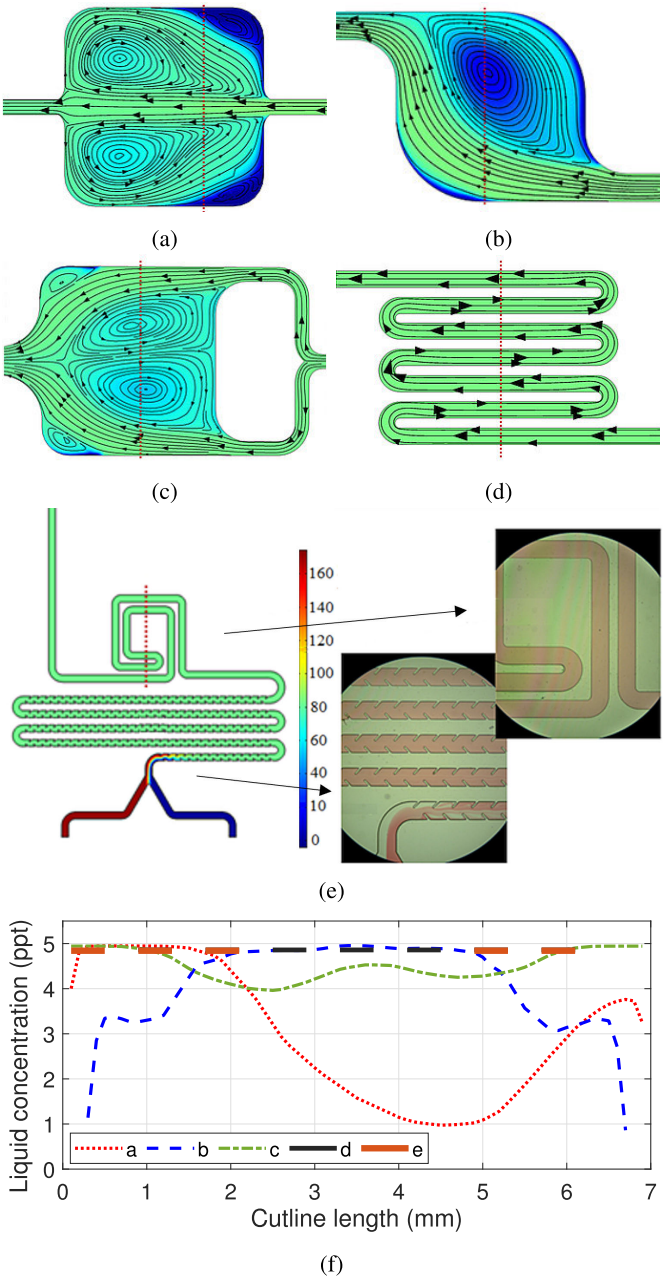

Fig. 4. Mixing simulations of 10-ppt saline water with distilled water for different fluidic geometries. Both fluids are introduced at the flow rate of 20 mL/h at each inlet. The mixing results are plotted at $t = 5$ s. (a)–(c) Distribution of the liquid concentration in the sensing area is not uniform. (d) and (e) Fluid concentration is constant along the channel. Photographs are taken during the operation of the mixer when uncolored and red dyed distilled water are introduced into inlet; the 20 times magnification of the mixing section and the sensing area is shown in the inset of (e). (f) Simulated concentration variation of saline solution along the cutline of each fluidic geometry.

because it provides an optimal layout as it guides the liquid properly and provides the most surface area in the near field of the CSRR. The mixture is collected from the outlet.

As a validation of the mixers, performance uncolored and red dyed distilled water are introduced into inlets A and B as it can be seen in the insets of Fig. 4(e). The volume ratio of the fluids is changed, as shown in Table II. The pressure of inlet A is increased, while the pressure of inlet

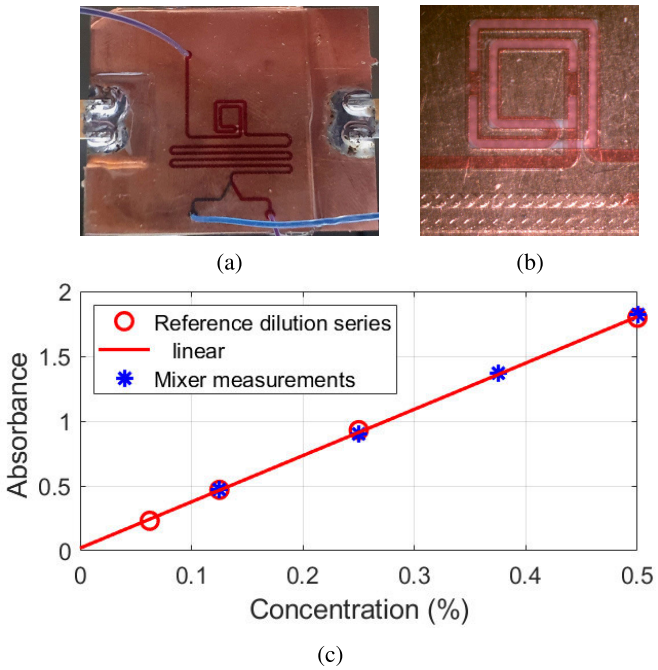

Fig. 5. (a) Photograph of the fully assembled device while colored liquids are mixed. (b) Sensing area is presented where the positioning of the microfluidic channel below the CSRR can be observed. (c) Performance of the mixer is verified by spectrophotometry.

TABLE II
SPECTROPHOTOMETRY RESULTS OF THE FLUID MIXING

Reference dilution series		Mixer measurements		
% sample	A	% sample	A	real value
0.5	1.797	0.5	1.822	0.5048
0.25	0.93	0.375	1.37	0.378
0.125	0.43	0.25	0.898	0.246
0.0625	0.231	0.125	0.473	0.1267

B is decreased in such a way that the total pressure is kept constant. The mixed fluid is collected from the outlet and it is measured by NanoDrop 2000 spectrophotometer at $\lambda = 495$ nm. Therefore, reference samples of dyed water with known concentration have been prepared and characterized with the spectrophotometer. The measured absorbance of the references can be fit with the linear regression

$$A = 3.568c + 0.02065 \quad (1)$$

where A is the absorbance and c is the concentration of dye. Then, the mixed fluid collected at the outlet of the mixer is characterized with the spectrophotometer. By reading the measured absorbance of the microfluidically mixed fluid, the concentration can be determined from the linear regression (see Fig. 5(c) and Table II). The maximum deviation between the reference and the microfluidic mixture is 1.6%, which proves the high accuracy of the mixing device.

III. FABRICATION AND MEASUREMENT SETUP

The proposed fluidic device consists of several layers as it is shown in Fig. 1(a). The parts of the device are fabricated with different processes. The microstrip transmission line with the CSRR on the ground plane is fabricated with conventional printed circuit board (PCB) technology. The microfluidic channels are fabricated by soft lithography. First, SU-8 2075 is dispensed onto a silicon wafer, which is then spin-coated at 2000 r/min for 30 s with an acceleration of 300 r/min/s in a Laurell WS-650MZ-23NPP spin coater. After the deposition of photoresist, the wafer is baked at 65 °C for 3 min and then at 95 °C for 8 min. The UV-light exposure is done by μPG101 direct laser writing machine. Postexposure baking is performed in three steps, first at 60 °C for 2 min, second at 95 °C for 7 min, and third at 60 °C for 2 min. During the development, three cycles of washing by SU-8 developer (10–5–2 min) and isopropanol (20–20–20 s) are applied to remove the uncured photoresist from the wafer. PDMS monomer and curing agent were mixed in the 10:1 ratio and then degassed in vacuum chamber. The mixture was poured onto the silicon mold to form a 2-mm-thick block, which was baked at 70 °C for 2 h to promote the curing process. Holes were punched into the peeled-off PDMS to form the inlets and the outlet of the channel. Then, the microfluidic channels are covered with borosilicate glass as follows. The 170-μm-thick borosilicate glass plate and the 2-mm-thick PDMS block containing the microfluidic channel are treated in oxygen plasma for 30 s. The treatment removes hydrocarbon groups, which allows Si–O–Si covalent bounds to form between glass and PDMS after stacking them [44]. Finally, the ground plane of the PCB is coated with 70-μm-thick PDMS layer, which glues the microfluidic chip in place. The channel is positioned below the CSRR with a stereomicroscope and the positioning accuracy can be observed in Fig. 5(b).

The schematics of the experimental arrangement, which includes the fluidic pump (Elveflow OB1 MK3+) and the microwave characterization setup, are presented in Fig. 6(a). After mixing, the outflowing liquid is collected in a glass. The photograph of the actual experimental setup is shown in Fig. 6(b). The change of the S_{21} transmission parameter is monitored with the Keysight vector network analyzer. In Fig. 6(c), the measured transmission parameter S_{21} is plotted when the channels are empty and when distilled water is pumped in both inlets of the mixer. The distilled water increases the effective permittivity in the sensing region, which leads to a downshift of the resonant peaks. For comparison, the transmission of the standalone CSRR without the fluidic layer is presented as well.

IV. CHARACTERIZATION OF THE DEVICE

The performance of the device is demonstrated by mixing saline water with different concentrations. As the electric permittivity of saline solutions is well known, therefore, this method is commonly used to characterize sensors [45]. In our case, this experiment is very convenient because it allows the joint characterization of microwave sensing and microfluidic mixing. First, the variation of the transmission parameter in a function of salinity is determined by pumping water of the same salinity into both inlets of the mixer. The pressure at the output of the pump is set to 1.9 bar. The salinity is modified in the range of 0 ppt (pure water) to 40 ppt with an increment of 10 ppt. The transmission parameter S_{21} of each saline sample is measured in the frequency range of 0–12 GHz, as it can be seen in Fig. 7. The variation of the measured transmission

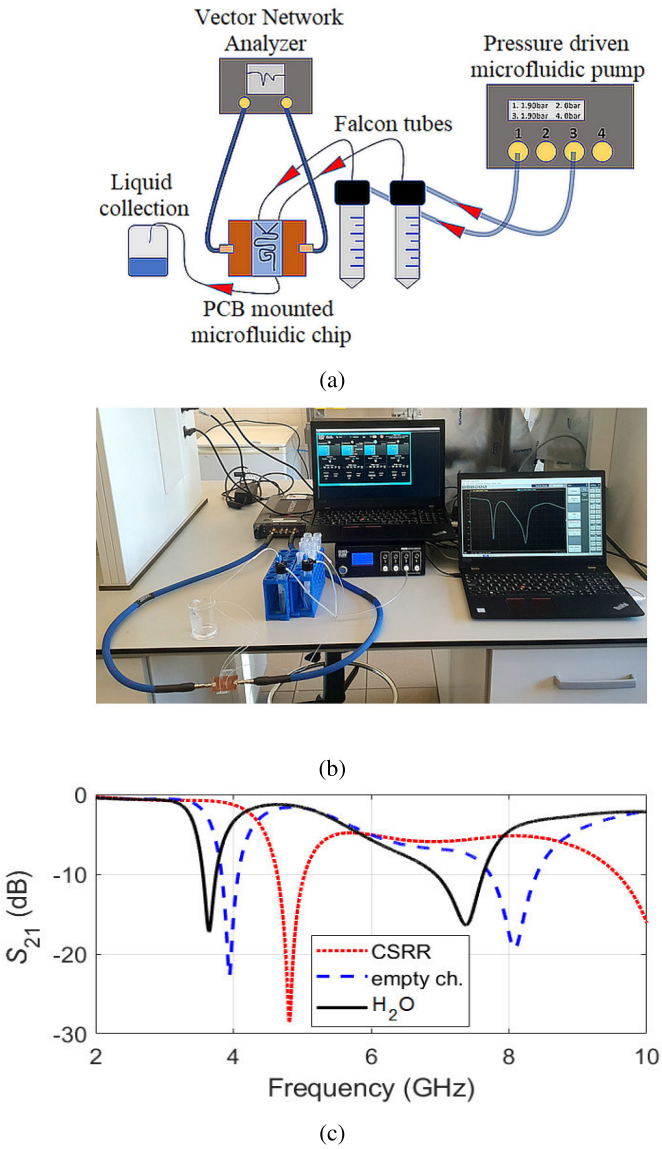

Fig. 6. (a) Schematics of the experimental setup. The liquids are introduced into the inlets of the mixer by a pressure-driven pump. After mixing, the outflowing liquid is collected in a glass. The transmission S_{21} of the sensor is monitored with the vector network analyzer. (b) Photograph of the experimental setup. (c) Measured S_{21} when the channels are empty and when distilled water is pumped in both inlets of the mixer. For comparison, the transmission of the standalone CSRR is also presented.

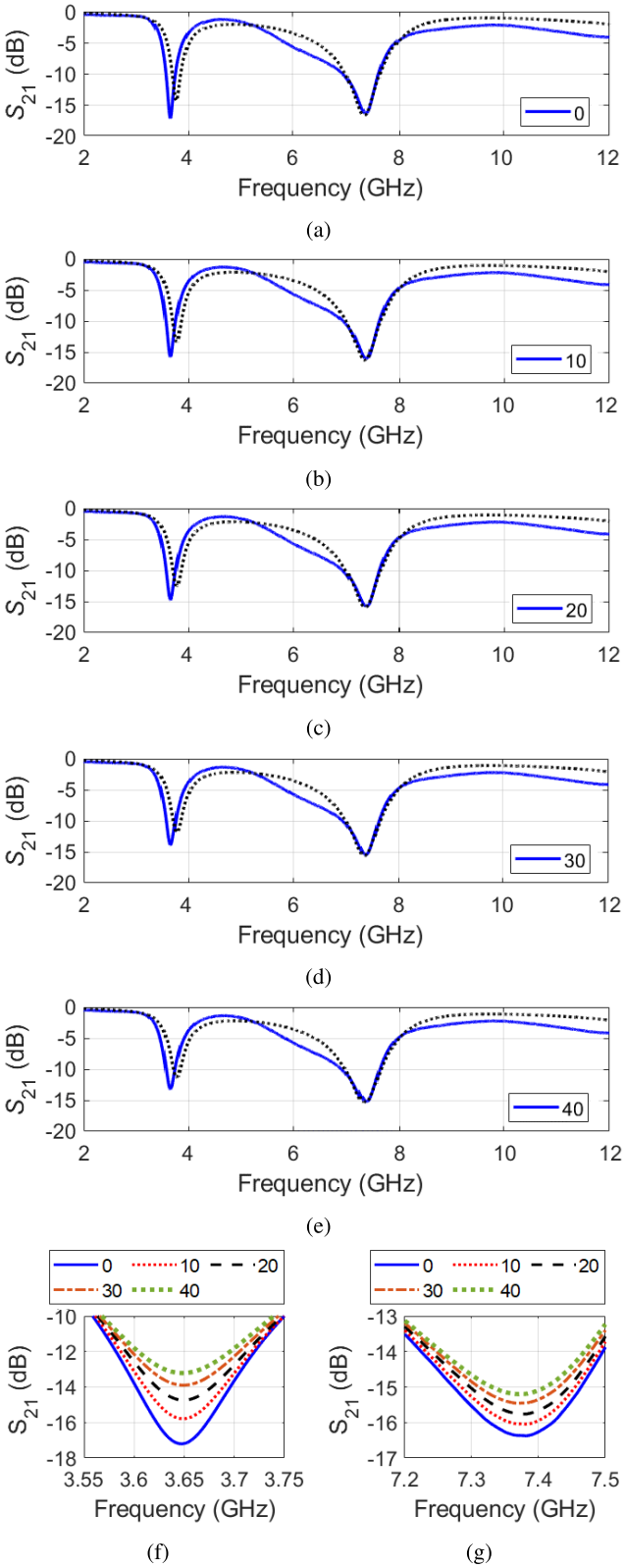

Fig. 7. (a)–(e) Measured (continuous line) and simulated (dotted line) S_{21} magnitudes for aqueous solutions of different salinity. (f) and (g) Measured transmission magnitudes in the frequency band of the first and second resonances, respectively.

parameter at the first and second resonances is magnified in Fig. 7(f) and (g). Note that the curves are well separated for both resonances. These data will serve as a reference to identify the concentration at the outlet when salty water of different concentration flows in the inlets.

Electromagnetic simulations of the full device with saline water of different concentrations flowing in the channels are also performed with the frequency-domain solver of CST Microwave Studio. In the simulations, the electric permittivity of PDMS is selected $\epsilon_r = 2.77$ and $\tan\delta = 0.024$ [46], [47]. The borosilicate glass cover of the fluidic channels is considered lossless with electric permittivity $\epsilon_r = 6.3$ [48]. At microwave frequencies, the electric permittivity of saline water can be expressed by extending the Debye model with an ionic conductive term [49]. The strongly dispersive and high-valued electric permittivity of water is the result of two

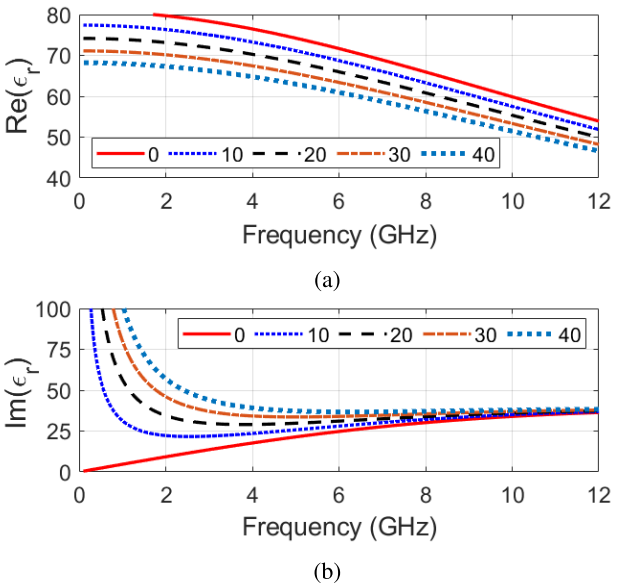

Fig. 8. Electric permittivity of saline water is highly dispersive. (a) Real part and (b) imaginary part of electric permittivity for different salinity (ppt) values at room temperature.

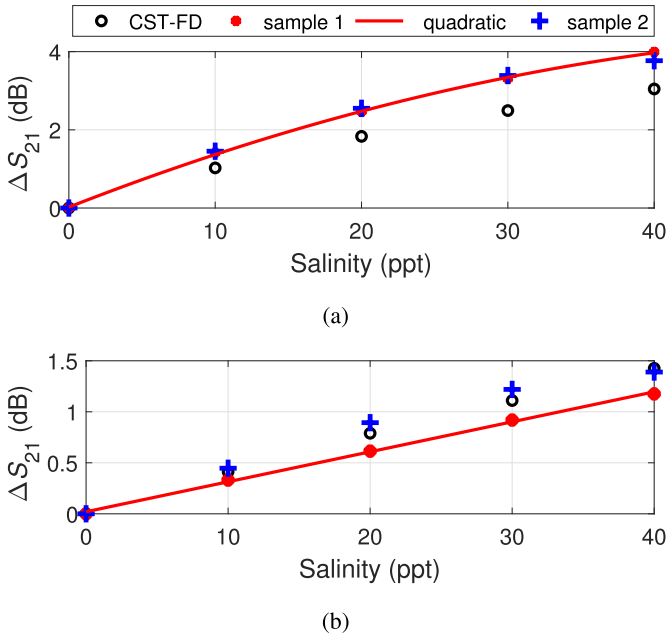

Fig. 9. Relative response of the mixing device in a function of salinity. (a) and (b) Variation of the S_{21} magnitude minima compared to pure water at the first and second resonances, respectively. Two samples are prepared and measured. The measured data are plotted with asterisk and plus sign markers, while the simulations result with circles. In (a) and (b), the variation of the measured data of sample 1 is fit with quadratic polynomial and linear regression, respectively.

counteracting effects. However, the permanent electric dipoles of water molecules align along the local electric field, and the thermal agitation works against this ordering. By mixing NaCl in water, freely moving ions are formed. Their electromagnetic contribution is considered with the additional ionic conductive term. The formulas of the model have been implemented as a CST Microwave Studio macro and are published online.[1] In the simulations, room temperature (24 °C) is assumed and the salinity is changed from 0 (pure water) to 40 ppt with an increment of 10 ppt. The corresponding variation of electric permittivity is shown in Fig. 8. In Fig. 7(a)–(e), the simulated S_{21} transmission parameters are plotted with dotted line and a good agreement between simulations and measurements can be observed.

As a function of the salinity, we determine the difference in the magnitude of the transmission at the resonant frequencies compared to the value obtained with distilled water. The differences are fit by polynomial expressions. The variation of ΔS_{21} at the first resonance in a function of salinity is plotted in Fig. 9(a) with asterisk and plus sign markers for two fabricated devices, and for comparison, the simulations are presented with circle markers. At the first resonance, there is a very good agreement between the measured and simulated data. The measured data of sample 1 can be fit with the quadratic polynomial

$$\Delta\,|S_{21}|_{\mathrm{dB}}^{f_1} = 1.193 \cdot 10^{-3} S^2 + 0.1464 S - 2.287 \cdot 10^{-2}. \quad (2)$$

The variation of ΔS_{21} at the second resonance in a function of salinity is plotted in Fig. 9(b). We have found that the second resonance is more sensitive to the thickness of the PDMS adhesive layer between the ground plane and the borosilicate glass layer, which may cause the difference of the two measured devices. In this case, the measured data of sample 1 can be fit with the linear regression

$$\Delta\,|S_{21}|_{\mathrm{dB}}^{f_2} = 2.939 \cdot 10^{-2} S + 2.005 \cdot 10^{-2}. \quad (3)$$

The fitting expressions can be easily inverted, which facilitates the readout of an unknown salinity form measured S_{21} data.

Then liquids of different concentrations are fed to the inlets of the mixer. Two examples are provided. In Fig. 10, the saline water of 20 ppt is mixed with 0 ppt (pure) water to produce 10-ppt saline water. In Fig. 10(a), the transmission parameter of the mixed solution is compared to the transmission parameter of Fig. 7(b) where, on both inlets of the mixer, 10-ppt saline water was pumped. In Fig. 10(b) and (c), the frequency regions around the first and second resonances are magnified, and for reference, the transmission spectra of 0- and 20-ppt saline water are plotted as well. The figures reveal that the performance of the microfluidic mixer and also the CSRR sensor measurement capability is outstanding. As it is shown in Fig. 10(d), the absolute error of the measurement is smaller than 0.5% everywhere.

In Fig. 11, the saline water of 20 ppt is mixed with 40-ppt saline water to produce 30-ppt saline water. In this case too, there is a very good agreement between the transmission spectra of the mixture and 30-ppt saline water; the measurement error is less than 0.4% everywhere, as it is plotted in Fig. 11(d).

Finally, the response for several chemicals manufactured by VWR Chemicals is measured and compared to the spectra of distilled water, as it is presented in Fig. 12. The sodium hydroxide solution (NaOH) is of 3.08%, the hydrochloric acid (HCl) is of 0.1 mol/l, the ethyl alcohol (C_2H_6O) has a

[1] [Online] Available: https://sourceforge.net/projects/fluidic-sensor/files/

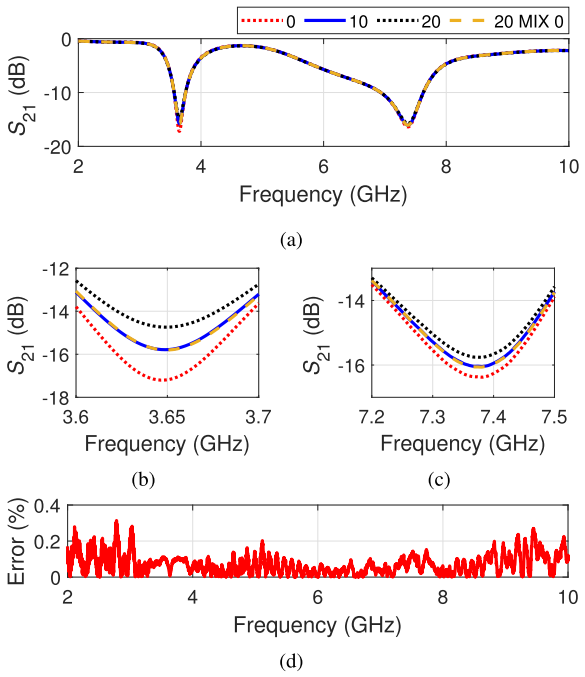

Fig. 10. Mixing 20 ppt saline water with pure water to produce 10 ppt saline water. (a) Measured transmission parameter of the mixture. For reference, the transmission parameter, when on both inlets of the mixer pure (0 ppt) water, 10 ppt saline water and 20 ppt saline water is pumped is plotted. (b) and (c) For a better observation the transmission spectra are magnified in the frequency region of the first and second resonance. (d) Absolute error of the measurement.

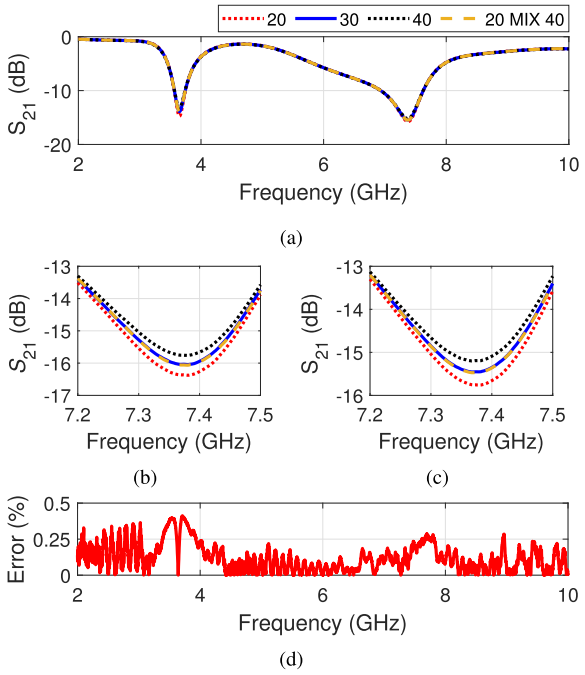

Fig. 11. Mixing 20 ppt saline water with 40 ppt saline water to produce 30-ppt saline water. (a) Measured transmission parameter of the mixture. For reference, the transmission parameter, when on both inlets of the mixer 20 ppt, 30-ppt and 40 ppt saline water is pumped is plotted. (b) and (c) For a better observation the transmission spectra are magnified in the frequency region of the first and second resonance. (d) Absolute error of the measurement.

concentration of 99.8%, and the isopropyl alcohol (C_3H_8O) is of 100%. The measurements demonstrate that these chemicals can be distinguished by simultaneous observation of the two

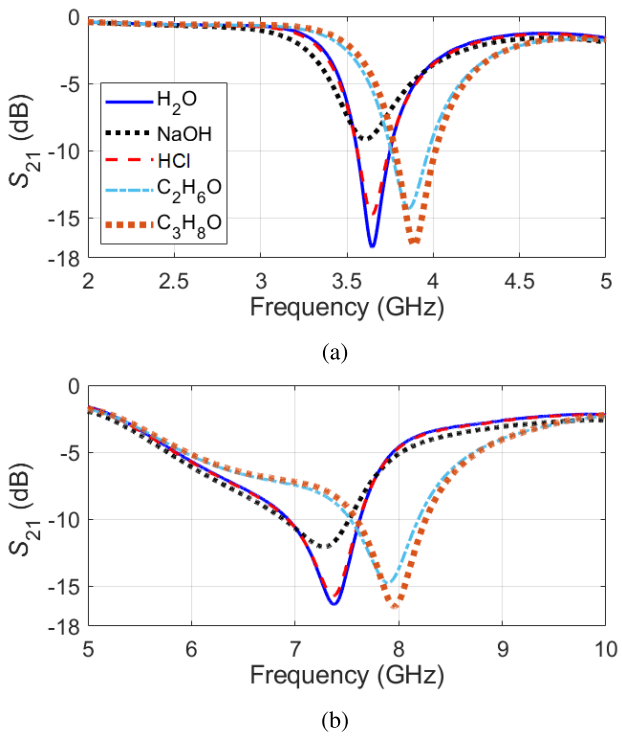

Fig. 12. Measured response for several chemicals. (a) and (b) Frequency region of the first and second resonance. The sodium hydroxide solution (NaOH) is of 3.08%, the hydrochloric acid (HCl) is of 0.1 mol/l, the ethyl alcohol (C_2H_6O) has a concentration of 99.8%, and the isopropyl alcohol (C_3H_8O) is of 100%.

resonant frequency shifts and the corresponding transmission magnitude variations.

V. Comparison With Other Sensors

To characterize microwave sensors, in several papers, the sensitivity is considered as the main parameter. Usually, it is defined as the resonant frequency shift or the change of the transmission or reflection amplitude in proportion to the difference of the electric permittivity, when the liquid under test (LUT) is present, with respect to a reference. The sensitivity of frequency shift ∇_f can be calculated as

$$\nabla_f = \frac{\left(f^{\text{ref}} - f\right)\epsilon_r^{\text{ref}}}{f^{\text{ref}}\left(\epsilon_r - \epsilon_r^{\text{ref}}\right)} \times 100 \tag{4}$$

where f is the resonant frequency when the LUT with electric permittivity ϵ_r fills the microfluidic channel in the sensing area and f^{ref} is the resonant frequency corresponding to empty channel or some reference fluid with electric permittivity ϵ_r^{ref}. However, this parameter is only partially suitable for characterizing microfluidic sensors, as the reference is not unique, and the definition does not consider the amount of sample to be detected, which can fill only partially the sensing region. In addition, there is no generally accepted rule for how to define the extent of the sensing region, neither the amount of the required sample. In our case, the sensing area is presented in the inset of Fig. 1(d), and only 1.5μL of fluid is required to fill the microfluidic channel of this region. Note that by including the channels of the mixing section and the connections also, the total amount of fluid required

TABLE III
SENSITIVITY OF FREQUENCY SHIFT

(a)

	f (GHz)	ϵ_r	f^{ref} (GHz)	ϵ_r^{ref}	∇_f (%)
first r.	3.646	75.84	3.943	1.0	0.10
second r.	7.380	69.21	8.084	1.0	0.13

Distilled water (H_2O) sample with reference to empty channel.

(b)

	f (GHz)	ϵ_r	f^{ref} (GHz)	ϵ_r^{ref}	∇_f (%)
first r.	3.857	10.14	3.943	1.0	0.24
second r.	7.892	6.14	8.084	1.0	0.46

Ethanol (C_2H_6O) sample with reference to empty channel.

(c)

	f (GHz)	ϵ_r	f^{ref} (GHz)	ϵ_r^{ref}	∇_f (%)
first r.	3.857	10.14	3.646	75.84	6.69
second r.	7.892	6.14	7.380	69.21	7.62

Ethanol (C_2H_6O) sample with reference to distilled water (H_2O).

TABLE IV
SENSITIVITY OF TRANSMISSION MAGNITUDE

	S_{21} (dB)	$\tan\delta$	S_{21}^{ref} (dB)	$\tan\delta_{ref}$	∇_{dB} (%)
first r.	-14.314	0.911	-17.203	0.933	3.94
second r.	-14.779	0.173	-16.375	0.349	5.82

Ethanol (C_2H_6O) sample with reference to distilled water (H_2O).

to operate the device is around 7.95 μL. Nevertheless, for a more complete characterization of the sensor, the sensitivity of frequency shift is calculated for distilled water with empty channel as a reference [see Fig. 6(c)], for ethanol with empty channel as a reference and for ethanol with distilled water as a reference [see Fig. 6(c)]. From the microfluidic point of view, distilled water is the more appropriate reference, as it is easier to wash than to clean-dry the channels between measurements. The data and the results of the calculations are summarized in Table III. The electric permittivity of ethanol is obtained from the two-term Debye dispersive formula [50].

The sensitivity of transmission magnitude variation ∇_{dB} can be defined as

$$\nabla_{\text{dB}} = \frac{\left(\left|S_{21}^{\text{ref}}\right| - |S_{21}|\right)\tan\delta_{\text{ref}}}{\left|S_{21}^{\text{ref}}\right|\left(\tan\delta - \tan\delta_{\text{ref}}\right)} \times 100 \tag{5}$$

where $|S_{21}|$ is the magnitude of transmission at the resonant frequency expressed in dB when the LUT with loss tangent $\tan\delta$ fills the microfluidic channel in the sensing area and $|S_{21}^{\text{ref}}|$ is the magnitude of transmission corresponding to the reference fluid with loss tangent $\tan\delta_{\text{ref}}$. The calculated sensitivities for ethanol with distilled water as a reference are presented in Table IV.

In Table V, several recently published resonance-based microwave sensor designs are compared. In Table V, the second column is the type of the sensor, where SRR, stepped impedance resonator (SIR), CSRR, metamaterial transmission line (MTL), and differential microwave sensor (DMS) are used as abbreviations. The third column shows the resonance frequency of the sensor. The fourth column lists the type of LUT. The fifth column is the required amount of LUT. The sixth column is the sensitivity, and however, the collected values are just indicative as they are calculated differently. Each of the tabulated sensor designs can have specific advantages, but

TABLE V
COMPARISON WITH OTHER DEVICES

Ref.	Type	f (GHz)	LUT	V (μL)	Sensitivity
[51]	SRR	1.86	Oil	subm.	3.04
[25]	SIR	1.91	Ethanol	0.637	NA
[29]	CSRR	2.226	Ethanol	0.52	0.98
[24]	MTL	2.6	Ethanol, Methanol	5	0.27
[30]	SRR	1.49, 1.72	Ethanol	0.68	1.43, 1.46
[54]	DMS	2.2	Glycerol	0.462	2.12
[55]	CSRR-patch	4.16	Ethanol	3	49.1 MHz/ϵ_r
[10]	4 CSRR	2.45	Glucose	600	0.63 MHz/mg/dL
[52]	SRR	0.752	Glucose	179.4	0.055 dB/g/L
TW	CSRR	3.65, 7.38	Saline water, Ethanol	1.5	3.94, 5.82 6.69, 7.62

neither of them is so outstanding as to be the favorite for microfluidic sensing. The microfluidic lab-on-a-chips can have complex densely packed geometries, therefore the designs of [24], [25], [30], [51], and [52], where the sensor and the feeding transmission line are located on the same side of the PCB that can make the integration difficult. Except for size reduction, the designs of [51] do not exploit the advantage of the double split-ring design, e.g., the possibility to work in two frequency bands. The design of [25] is complicated because vias are required, which makes the scaling of the device to higher frequencies difficult. The design of [29] works in only one frequency band and the scaling of the devices is also limited due to the meandered section of the CSRR; the same applies to [30] where interdigital capacitance is utilized. In [24], an MTL couples to an SRR. Two Teflon tubes, which serve as inlets, connect in a Y-junction to a third tube, which is positioned in the most sensitive area of the SRR, that is, the region of the coupling gap. However, due to microfluidic principles, this setup cannot guarantee that the two fluids will be mixed. Measurement setups, which are accurate, but require additional reference arms [52], [53], are avoided because they require the redesign of existing fluidic chip geometries and also increase the complexity of fluidic instrumentation. Due to coupling between the elements, the four CSRRs of [10] reduce the resonator sizes, however at the expense of increase of the sensing region, consequently of the required sample volume. The tabulated designs utilize a straight segment of fluidic channel [24], [25], [29] and a reservoir [10], [30] or it is simply immersed in the LUT [51]. The sensitivity of these sensors is increased only by electromagnetic principles, and none of them consider microfluidic requirements. Our conformal channel, which matches the high electric field regions of the double CSRR, increases the sensitivity in the frequency regions of the two resonances compared to a straight channel. At the same time, the volume of the required LUT is minimized and unwanted microfluidic mixing is eliminated.

VI. CONCLUSION

A novel general-purpose microfluidic mixing device, which is integrated with a microwave sensor, has been proposed. The multiphysics design procedure, which includes

electromagnetic and fluid dynamics simulations has been presented. The details of the fabrication procedure have been described and working prototypes have been fabricated and measured. Special care has been taken to design the microfluidic channel geometry in the sensing area. This is primarily important for the operation of the sensor because this way unwanted fluid mixing and the accumulation of air bubbles in the sensing area are avoided; therefore, insignificant and wrong data readouts are eliminated. The selected layout is optimal as it guides the liquid properly and at the same time provides the most surface area in the near field of the CSRR, which is necessary to achieve a good sensor sensitivity. The performance of the mixing device is demonstrated by pumping saline water of different concentrations to the inlets of the device. The measured transmission spectra of the mixed fluids reveal that the performance of the microfluidic mixer and the CSRR sensor measurement capability are outstanding, and the absolute error is smaller than 0.5%. The transmission spectra for several chemicals are also measured, which shows that simultaneous observation of the two resonance frequency shift and transmission magnitude variation allows not only detection of change in properties, e.g., concentration, but also unique identification of mixed fluids.

REFERENCES

[1] D. Li, *Encyclopedia of Microfluidics and Nanofluidics*. New York, NY, USA: Springer, 2008.

[2] C. Kleinstreuer, *Microfluidics and Nanofluidics: Theory and Selected Applications*. Hoboken, NJ, USA: Wiley, 2013.

[3] I. H. Woodhouse, Ed., *Introduction to Microwave Remote Sensing*. Boca Raton, FL, USA: CRC Press, 2017.

[4] J. Naqui and F. Martin, "Transmission lines loaded with bisymmetric resonators and their application to angular displacement and velocity sensors," *IEEE Trans. Microw. Theory Techn.*, vol. 61, no. 12, pp. 4700–4713, Dec. 2013.

[5] S. Guha, F. I. Jamal, and C. Wenger, "A review on passive and integrated near-field microwave biosensors," *Biosensors*, vol. 7, no. 4, p. 42, Sep. 2017.

[6] J. C. M. Hwang, "Label-free noninvasive cell characterization: A methodology using broadband impedance spectroscopy," *IEEE Microw. Mag.*, vol. 22, no. 5, pp. 78–87, May 2021.

[7] G. Petropoulos, Ed., *Remote Sensing of Energy Fluxes and Soil Moisture Content*. Boca Raton, FL, USA: CRC Press, 2013.

[8] N. Jankovic and V. Radonic, "A microwave microfluidic sensor based on a dual-mode resonator for dual-sensing applications," *Sensors*, vol. 17, no. 12, p. 2713, Nov. 2017.

[9] N. Celik, R. Gagarin, G. C. Huang, M. F. Iskander, and B. W. Berg, "Microwave stethoscope: Development and benchmarking of a vital signs sensor using computer-controlled phantoms and human studies," *IEEE Trans. Biomed. Eng.*, vol. 61, no. 8, pp. 2341–2349, Aug. 2014.

[10] A. E. Omer et al., "Low-cost portable microwave sensor for non-invasive monitoring of blood glucose level: Novel design utilizing a four-cell CSRR hexagonal configuration," *Sci. Rep.*, vol. 10, no. 1, pp. 1–20, Sep. 2020.

[11] E. L. Chuma and T. Rasmussen, "Metamaterial-based sensor integrating microwave dielectric and near-infrared spectroscopy techniques for substance evaluation," *IEEE Sensors J.*, vol. 22, no. 20, pp. 19308–19314, Oct. 2022.

[12] L. Zhang and A. M. Niknejad, "Design and analysis of a microwave-optical dual modality biomolecular sensing platform," *IEEE J. Solid-State Circuits*, vol. 55, no. 3, pp. 639–649, Mar. 2020.

[13] X. Zhu, W. Guo, F. Kang, F. Kong, and Q. Zhu, "Determination of protein content of raw fresh cow's milk using dielectric spectroscopy combined with chemometric methods," *Food Bioprocess Technol.*, vol. 9, no. 12, pp. 2092–2102, Dec. 2016.

[14] Southwest Microwave. *Dual Technology Motion Sensor*. Accessed: Mar. 22, 2023. [Online]. Available: https://www.southwestmicrowave.com/pdfs/MS15-MS16-Data-Sheet-EN.pdf

[15] R. Marqués, F. Martín, and M. Sorolla, *Metamaterials With Negative Parameters*. Hoboken, NJ, USA: Wiley, 2008.

[16] L. Solymár and E. Shamonina, *Waves in Metamaterials*. London, U.K.: Oxford Univ. Press, 2009.

[17] F. Martín, J. Bonache, F. Falcone, M. Sorolla, and R. Marqués, "Split ring resonator-based left-handed coplanar waveguide," *Appl. Phys. Lett.*, vol. 83, no. 22, pp. 4652–4654, Dec. 2003.

[18] F. Falcone, T. Lopetegi, J. D. Baena, R. Marques, F. Martin, and M. Sorolla, "Effective negative-ϵ stopband microstrip lines based on complementary split ring resonators," *IEEE Microw. Wireless Compon. Lett.*, vol. 14, no. 6, pp. 280–282, Jun. 2004.

[19] J. Naqui, M. Durán-Sindreu, and F. Martín, "Alignment and position sensors based on split ring resonators," *Sensors*, vol. 12, no. 9, pp. 11790–11797, Aug. 2012.

[20] M. S. Boybay and O. M. Ramahi, "Material characterization using complementary split-ring resonators," *IEEE Trans. Instrum. Meas.*, vol. 61, no. 11, pp. 3039–3046, Nov. 2012.

[21] C.-S. Lee and C.-L. Yang, "Complementary split-ring resonators for measuring dielectric constants and loss tangents," *IEEE Microw. Wireless Compon. Lett.*, vol. 24, no. 8, pp. 563–565, Aug. 2014.

[22] S. A. Alotaibi, Y. Cui, and M. M. Tentzeris, "CSRR based sensors for relative permittivity measurement with improved and uniform sensitivity throughout [0.9–10.9] GHz band," *IEEE Sensors J.*, vol. 20, no. 9, pp. 4667–4678, May 2020.

[23] C.-M. Hsu and C.-L. Yang, "High sensitive detection of flow rate and permittivity through microfluidics based on complementary split-ring resonators," in *IEEE MTT-S Int. Microw. Symp. Dig.*, Jun. 2017, pp. 1015–1017.

[24] M. Abdolrazzaghi, M. Daneshmand, and A. K. Iyer, "Strongly enhanced sensitivity in planar microwave sensors based on metamaterial coupling," *IEEE Trans. Microw. Theory Techn.*, vol. 66, no. 4, pp. 1843–1855, Apr. 2018.

[25] A. Ebrahimi, J. Scott, and K. Ghorbani, "Ultrahigh-sensitivity microwave sensor for microfluidic complex permittivity measurement," *IEEE Trans. Microw. Theory Techn.*, vol. 67, no. 10, pp. 4269–4277, Oct. 2019.

[26] P. Vélez, K. Grenier, J. Mata-Contreras, D. Dubuc, and F. Martín, "Highly-sensitive microwave sensors based on open complementary split ring resonators (OCSRRs) for dielectric characterization and solute concentration measurement in liquids," *IEEE Access*, vol. 6, pp. 48324–48338, 2018.

[27] G. Acevedo-Osorio, E. Reyes-Vera, and H. Lobato-Morales, "Dual-band microstrip resonant sensor for dielectric measurement of liquid materials," *IEEE Sensors J.*, vol. 20, no. 22, pp. 13371–13378, Nov. 2020.

[28] E. L. Chuma, Y. Iano, G. Fontgalland, L. L. B. Roger, and H. Loschi, "PCB-integrated non-destructive microwave sensor for liquid dielectric spectroscopy based on planar metamaterial resonator," *Sens. Actuators A, Phys.*, vol. 312, Sep. 2020, Art. no. 112112.

[29] L.-C. Fan, W.-S. Zhao, D.-W. Wang, Q. Liu, S. Chen, and G. Wang, "An ultrahigh sensitivity microwave sensor for microfluidic applications," *IEEE Microw. Wireless Compon. Lett.*, vol. 30, no. 12, pp. 1201–1204, Dec. 2020.

[30] W. Ye, D.-W. Wang, J. Wang, G. Wang, and W.-S. Zhao, "An improved split-ring resonator-based sensor for microfluidic applications," *Sensors*, vol. 22, no. 21, p. 8534, Nov. 2022.

[31] S. Hossain, M. A. Ansari, and K.-Y. Kim, "Evaluation of the mixing performance of three passive micromixers," *Chem. Eng. J.*, vol. 150, nos. 2–3, pp. 492–501, Aug. 2009.

[32] A. Alam and K.-Y. Kim, "Analysis of mixing in a curved microchannel with rectangular grooves," *Chem. Eng. J.*, vols. 181–182, pp. 708–716, Feb. 2012.

[33] J. Li, G. Xia, and Y. Li, "Numerical and experimental analyses of planar asymmetric split-and-recombine micromixer with dislocation sub-channels: Planar asymmetric split-and-recombine micromixer with dislocation sub-channels," *J. Chem. Technol. Biotechnol.*, vol. 88, no. 9, pp. 1757–1765, Sep. 2013.

[34] M. A. Ansari and K.-Y. Kim, "Parametric study on mixing of two fluids in a three-dimensional serpentine microchannel," *Chem. Eng. J.*, vol. 146, no. 3, pp. 439–448, Feb. 2009.

[35] S. Hossain, I. Lee, S. M. Kim, and K.-Y. Kim, "A micromixer with two-layer serpentine crossing channels having excellent mixing performance at low Reynolds numbers," *Chem. Eng. J.*, vol. 327, pp. 268–277, Nov. 2017.

[36] ISOLA Group. *IS680-345*. Accessed: Dec. 10, 2022. [Online]. Available: https://www.isola-group.com/pcb-laminates-prepreg/is680-laminate/

[37] J. B. Pendry, A. J. Holden, D. J. Robbins, and W. J. Stewart, "Magnetism from conductors and enhanced nonlinear phenomena," *IEEE Trans. Microw. Theory Techn.*, vol. 47, no. 11, pp. 2075–2084, Nov. 1999.

[38] B. Sauviac, C. R. Simovski, and S. A. Tretyakov, "Double split-ring resonators: Analytical modeling and numerical simulations," *Electromagnetics*, vol. 24, no. 5, pp. 317–338, Jan. 2004.

[39] F. Rachford, D. L. Smith, and P. F. Loschialpo, "Experiments and simulations of microwave negative refraction in split ring and wire array negative index materials, 2D split-ring resonator and 2D metallic disk photonic crystals," in *Physics of Negative Refraction and Negative Index Materials* (Springer Series in Materials Science), vol. 98. Berlin, Germany: Springer, Jan. 2007.

[40] F. Hesmer et al., "Coupling mechanisms for split ring resonators: Theory and experiment," *Phys. Status Solidi B*, vol. 244, no. 4, pp. 1170–1175, Apr. 2007.

[41] H. Guo et al., "Resonance hybridization in double split-ring resonator metamaterials," *Opt. Exp.*, vol. 15, no. 19, pp. 12095–12101, Sep. 2007.

[42] J. D. Baena et al., "Equivalent-circuit models for split-ring resonators and complementary split-ring resonators coupled to planar transmission lines," *IEEE Trans. Microw. Theory Techn.*, vol. 53, no. 4, pp. 1451–1461, Apr. 2005.

[43] Z. Szabó, "Dual band CSRR fluidic sensor with 3D printed channel," in *Proc. 52nd Eur. Microw. Conf. (EuMC)*, Sep. 2022, pp. 524–527.

[44] S. Bhattacharya, A. Datta, J. M. Berg, and S. Gangopadhyay, "Studies on surface wettability of poly(dimethyl) siloxane (PDMS) and glass under oxygen-plasma treatment and correlation with bond strength," *J. Microelectromech. Syst.*, vol. 14, no. 3, pp. 590–597, Jun. 2005.

[45] A. Ebrahimi, J. Scott, and K. Ghorbani, "Highly sensitive microwave-based biosensor for electrolytic level measurement in water," in *Proc. IEEE Asia–Pacific Microw. Conf. (APMC)*, Dec. 2019, pp. 759–761.

[46] P.-Y. Cresson et al., "1 to 220 GHz complex permittivity behavior of flexible polydimethylsiloxane substrate," *IEEE Microw. Wireless Compon. Lett.*, vol. 24, no. 4, pp. 278–280, Apr. 2014.

[47] P. K. Sharma, N. Gupta, and P. I. Dankov, "Analysis of dielectric properties of polydimethylsiloxane (PDMS) as a flexible substrate for sensors and antenna applications," *IEEE Sensors J.*, vol. 21, no. 17, pp. 19492–19504, Sep. 2021.

[48] *The Electric Permittivity of the Borosilicate Glass*. Accessed: Dec. 10, 2022. [Online]. Available: https://web.mit.edu/sriram/Public/Graphics/Sylgard184Datasheet.pdf

[49] A. Stogryn, "Equations for calculating the dielectric constant of saline water (correspondence)," *IEEE Trans. Microw. Theory Techn.*, vol. MTT-19, no. 8, pp. 733–736, Aug. 1971.

[50] E. Moctezuma-Pascual, G. Méndez-Jerónimo, Z. O. Rodríguez-Moré, H. Lobato-Morales, and R. Torres-Torres, "Microwave characterization of liquid samples through the systematic parameter extraction of the circuit equivalence for the Debye model," *IEEE Microw. Wireless Compon. Lett.*, vol. 30, no. 1, pp. 116–119, Jan. 2020.

[51] G. Galindo-Romera, F. J. Herraiz-Martínez, M. Gil, J. J. Martínez-Martínez, and D. Segovia-Vargas, "Submersible printed split-ring resonator-based sensor for thin-film detection and permittivity characterization," *IEEE Sensors J.*, vol. 16, no. 10, pp. 3587–3596, May 2016.

[52] P. Vélez, J. Mata-Contreras, D. Dubuc, K. Grenier, and F. Martín, "Solute concentration measurements in diluted solutions by means of split ring resonators," in *Proc. 48th Eur. Microw. Conf. (EuMC)*, Sep. 2018, pp. 231–234.

[53] A. Ebrahimi, J. Scott, and K. Ghorbani, "Differential sensors using microstrip lines loaded with two split-ring resonators," *IEEE Sensors J.*, vol. 18, no. 14, pp. 5786–5793, Jul. 2018.

[54] A. Ebrahimi, F. J. Tovar-Lopez, J. Scott, and K. Ghorbani, "Differential microwave sensor for characterization of glycerol–water solutions," *Sens. Actuators B, Chem.*, vol. 321, Oct. 2020, Art. no. 128561.

[55] A. Salim and S. Lim, "Complementary split-ring resonator-loaded microfluidic ethanol chemical sensor," *Sensors*, vol. 16, no. 11, p. 1802, Oct. 2016.